Thermal ageing effect on solute segregation and precipitation in the heat-affected-zone of dissimilar metal welds for nuclear power plants

I Medouni, A Portavoce, P Maugis, M Descoins, M Yescas, F Roch, P Joly, K Hoummada

Materials & Design 232 (2023) 112158

Contents lists available at ScienceDirect

Materials & Design

journal homepage: www.elsevier.com/locate/matdes

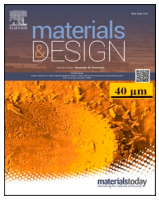

Thermal ageing effect on solute segregation and precipitation in the heat-affected-zone of dissimilar metal welds for nuclear power plants

I. Medouni [a,b], A. Portavoce [a,*], P. Maugis [a], M. Descoins [a], M. Yescas [b], F. Roch [b], P. Joly [b], K. Hoummada [a]

[a] Aix Marseille Univ, CNRS, Université de Toulon, IM2NP, FSCM, CP2M 13397, Marseille, France
[b] Framatome, Développement (DTID) et Ingénierie Mécanique (DTIM), 92084 Paris La Défense CEDEX, France

ARTICLE INFO

Keywords:
Long-term thermal ageing
Grain boundary
Segregation
Precipitation
Heat affected zone

ABSTRACT

Solute segregation in the carbon-depleted (CDZ) heat-affected zone of dissimilar metal welds (DMW) designed for nuclear power plant EPR^{TM} reactors has been investigated by atom probe tomography (APT) and related to the mechanical properties (toughness test). The analysis of grain boundaries (GBs) by APT allowed the quantification of the P segregation and other solute elements, in all the analyzed samples, before and after long-term ageing heat treatments. The post-weld stress-relief heat treatment applied to the samples before the ageing heat treatments leads to important GBs segregation levels. Following thermal ageing treatments allow a relative increase of GB segregation. P segregation increases with the various thermal ageing conditions. The experimental data were used to model P segregation in high-angle GBs. The simulations show that P segregation is kinetically limited by bulk diffusion, explaining the observed P segregation increase with temperature. P segregation in GBs in the CDZ of the DMW should remain low compared to the expected equilibrium segregation level during the entire reactor service. In addition to solute segregation in extended defects, APT measurements revealed the presence of Cu-rich clusters in GBs, dislocations, and grains in all the aged samples. These clusters were not observed in the sample before ageing.

1. Introduction

Usually, solute atom segregation on grain boundaries (GBs) affects polycrystalline material properties [1]. This segregation may either improve or weaken interface cohesion, and therefore the mechanical properties depending on the nature of the segregated solute atoms. Generally, a well-known example is temper-embrittlement by phosphorous segregation at ferrite GBs. In contrast, carbon GB segregation improves GB cohesion [2]. Phosphorous GB segregation was reported during the thermal ageing of dissimilar metal welds (DMW), and is thus suspected to be the cause of intergranular fracture after thermal ageing [3–5]. Indeed, a new narrow gap design of DMW for nuclear plants has been recently developed. These DMWs are used to join the main components of the nuclear island made of low-alloy steel (LAS) with the main coolant line pipes made of austenitic stainless steel of type 304L. The filler metal used to join both steels is the nickel-based alloy ER Ni-Cr-Fe-7 (Inconel 52®), which is deposited using only one pass per layer by the gas tungsten arc welding (GTAW) process. Further details about the design of these DMWs can be found elsewhere [6,7].

During the post-weld stress-relief heat treatment (SRHT) performed at 610 °C for several hours on these DMWs, carbon migrates from the heat affected zone (HAZ) of the LAS to the nickel-based alloy weld metal. This leads to the formation of a carbon-depleted zone (CDZ) within the HAZ with particular features in terms of microstructure and mechanical properties. Such features are due to the dissolution of the majority of the carbide precipitates obtained after the quench and temper-treatments carried out during the manufacturing process, modifying the original bainitic microstructure [3]. Despite these microstructure evolutions of the weld joint, an important thermal ageing research program has shown that the fracture toughness in the ductile-to-brittle temperature domain of testing in the LAS carbon-depleted zone is still satisfactory, even at the end of the nuclear reactor design life (60 years), at all operating temperatures, including those for the pressurizer (around 350 °C) [3]. However, in order to improve our understanding of thermal ageing mechanisms, from a metallurgical point of view, investigations of GB properties were also launched.

* Corresponding author.
E-mail address: alain.portavoce@im2np.fr (A. Portavoce).

https://doi.org/10.1016/j.matdes.2023.112158
Received 23 March 2023; Received in revised form 23 June 2023; Accepted 9 July 2023
Available online 13 July 2023

The intergranular embrittlement of the CDZ during long-term thermal ageing treatments is suspected to be mainly due to phosphorous segregation at GBs. Indeed, numerous studies [8–13] have linked intergranular embrittlement with GB phosphorous segregation. However, it is well established that elements other than Phosphorus, such as Copper, Zinc, Silicon, Sulphur, Oxygen, Nickel, and Manganese, can also promote intergranular weakness in iron [2,14]. In contrast, GB segregation of Molybdenum and Carbon is known to improve intergranular cohesion. Thus, it is important to know which elements, apart from phosphorous, segregate to the GBs in the CDZ, and to quantify their segregation. Phosphorous segregation at GBs is often studied using Auger electron spectroscopy (AES) on the intergranular surfaces obtained by in-situ GB fracture [15,16]. However, accurate atomic compositions are difficult to be obtained with this technique, since the AES signal is dependent on many factors, and its best detection limit is generally not better than 1 at% [17].

In addition, in the case of the CDZ of DMWs, the morphology of ferritic GBs is modified due to carbide dissolution and microstructural changes which lead to local grain growth, resulting in GBs with jagged or irregular shapes. Therefore, sharp intergranular fracture is more difficult to achieve, limiting GB composition investigations by AES. Atom probe tomography (APT) is more appropriate in this case, allowing for atomic scale quantification of all the solute atoms segregated on both, dislocations and grain boundaries [18–20].

2. Materials and experimental techniques

DMW are used in nuclear power plants, in particular for the constitution of the primary circuit, for joining primary pipes made of austenitic stainless steel Fig. 1.***a***. The steels analyzed in this study are part of DMW representative mock-ups made of an austenitic steel (304L type) and a low-alloy steel (18MND5 type) Fig. 1.***b***, welded together by a nickel-based alloy ER Ni-Cr-Fe-7 (Inconel 52®).

In this paper, we will only focus on the HAZ of the 18MND5 steel part of the weld joint Fig. 1.***c***. The nominal composition of the LAS studied in this paper is indicated in Table 1.

Two representative mock-ups were welded, namely mock-up MC4 and mock-up MC-2807. After welding, these two mock-ups were submitted to a SRHT (610 °C for 16 h) aimed for relieving the residual stress created in the DMW due to the welding process. This SRHT was followed by a furnace in-situ cooling down to 350 °C, at a cooling rate of 30 °C/h, and then to air cooling down to room temperature. Once the SRHT was completed, different long-term accelerated thermal ageing treatments were applied to blanks taken from the mock-ups. The Table 2 summarizes the long-term thermal ageing conditions of the five investigated specimens.

Samples' microstructure was studied using scanning electron microscopy (SEM) in a XL-30 setup from FEI using a beam energy of 5 kV. The polycrystalline structure of the investigated LAS region was characterized by Electron backscatter diffraction (EBSD) using an (EDAX) Hikari Super camera in a ZEISS Gemini 500 field emission gun SEM. Orientation maps were collected using: a 12.34 mm work distance, a 0.08 μm step size, and a 20 kV voltage. Post-processing was performed using the Orientation Imaging Microscopy (OIM) program [21,22].

APT volumes of all the samples were acquired using a CAMECA LEAP 3000XHR setup in electric mode. The analyses were performed at 80 K with a pulse rate of 200 kHz. The pulse fraction was set to 20 % and the evaporation rate to 0.2 %/pulse. APT sample preparation was carried out using a dual beam SEM/FIB FEI Helios NanoLab 600. The samples (i.e. tips) were prepared using a standard lift-out method, followed by annular milling [23]. The reconstruction mode used to process APT data is voltage, with an evaporation field of 33 Vnm^{-1} representative of iron. The k factor is 3,3. The interfacial excess number (N_{ex}) was determined for each of the different species from APT measurements in order to quantify their GB segregation. N_{ex} is calculated by integrating the difference between the local concentration $N(z)$ measured across the considered GB and the bulk concentration N^{∞} measured far from the GB ***(Eq. (1))*** [24].

$$N_{ex} = \int_{-L/2}^{+L/2} (N(z) - N^{\infty})dz \quad (1)$$

The tips were prepared from wedges retrieved in the CDZ, at a distance between 5 and 15 μm from the 18MND5 LAS/Inconel 52® interface, for the five analyzed specimens. For the MC4-B specimen, tips were also prepared from a region located in at 200 μm away from the fusion line.

Fracture toughness tests were carried out with the crack tip precisely located in the ferritic HAZ, as close as possible to the fusion line (18MND5/ Inconel 52® interface). The tests were done on the sample MC4 after the SRHT (MC4–A), and on the sample MC4 aged at T = 400 °C for 10000 h [3].

3. Results

The toughness results showed that the ductile–brittle transition temperatures were still good (transition temperatures < T = − 100 °C) after long-term thermal ageing, but a shift in the ductile–brittle transition temperature of about 30 °C was nevertheless observed. The analysis

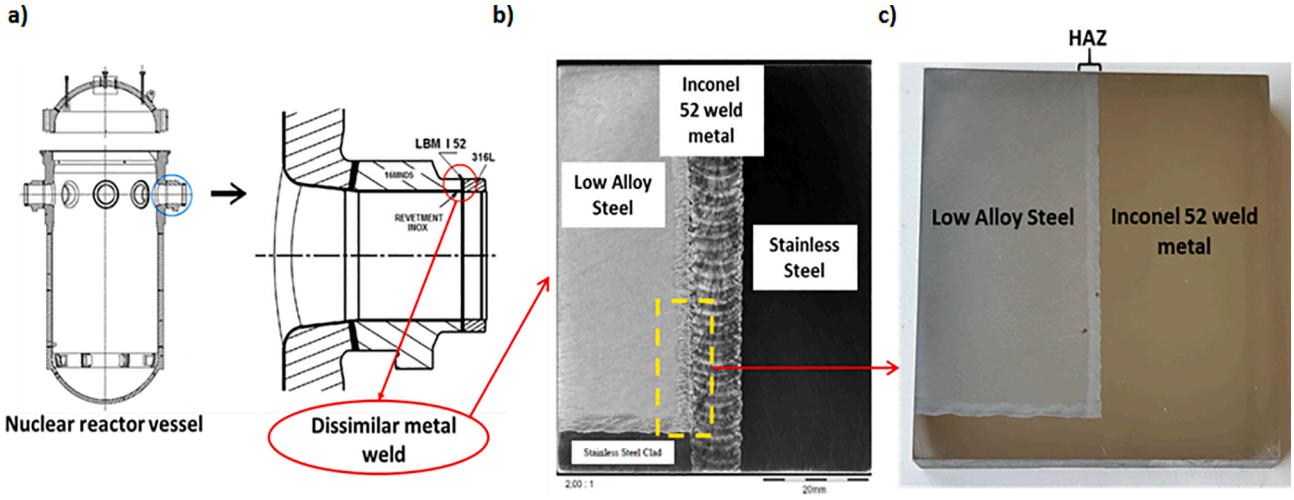

Fig. 1. Origin of the studied samples. a) illustration of a nuclear reactor vessel and its connections with the dissimilar weld of the present study [4]; b) Macrograph of a section of one of the Narrowgap TIG Alloy 52 DMW of the present study (MC4 mock up) [3]. c) sample extracted from the weld joint presented in b).

Table 1
Nominal composition of the low-alloy steel (18MND5 type).

	Fe	Mn	C	Ni	Si	Mo	Cr	Cu	Al	P	S	Co	As
at.%	96.39	1.48	0.872	0.68	0.413	0.285	0.163	0.086	0.037	0.013	0.01	0.01	0.007
wt.%	96.63	1.46	0.188	0.712	0.208	0.491	0.152	0.098	0.018	0.007	0.006	0.011	0.01

Table 2
Accelerated long-term thermal ageing heat treatments applied on the specimens taken from the ferritic side of the DMW representative mock-ups, specimen MC4-A was analysed in the initial condition, i.e. after SRHT.

	MC4-A	MC4-B	MC-2807	MC4-C	MC4-D
SRHT	610 °C/16 h				
Ageing	none	350 °C/50 000 h	400 °C/10 000 h	400 °C/30 000 h	450 °C/5 000 h

of the fractured surface revealed that the fracture was of intergranular type and occurred in the CDZ of the LAS [3]. These results motivated the GB segregation investigation in the CDZ by APT (Section 3.1).

The microstructure of the sample MC4–A is presented in Fig. 2.***a***. As observed, microstructure changes occurred during the SRHT. First, the carbides were dissolved in a bainite region comprised up to a distance of 100 μm from 18MND5/ Inconel 52® interface. As explained using finite volume simulations in a previous work [3], the bainite phase is in thermodynamic equilibrium with the Inconel 52® austenitic phase. Due to the high temperature (610 °C) and the high chromium content of the Inconel 52®, the iron carbide precipitates get dissolved, and the carbon atoms diffuse toward the 18MND5/Inconel 52® interface to form chromium-rich carbide precipitates.

Second, peculiar morphologies of grains and GBs can be observed in the CDZ (Fig. 2.***b***). The grains are larger and the GBs are irregular. This microstructure can be explained by grain growth due to GB free motion promoted by the dissolution of the carbides initially pining the GBs in the CDZ. EBSD analyses were also carried out in the CDZ of the sample MC4–A (Fig. 2.***c***). The GB disorientation distribution extracted from the EBSD analysis is given in Fig. 2.***d***. As commonly admitted, GBs can be categorized into two categories depending on the disorientation angle noted θ. Low-angle grain boundaries (LAGB) correspond to $\theta \leq 15°$ and high-angle grain boundaries (HAGB) correspond to $\theta > 15°$ [25,26]. In the present case, the GB distribution mostly contains HAGBs, the LAGB proportion being 40%.

Furthermore, 50% of these HAGBs exhibit $\theta > 30°$. This GB distribution is in agreement with the distribution determined by Eghbali [27] for plain low-carbon ferritic steel. According to our observations, this microstructure is not modified by the different subsequent ageing heat treatments. Only the solute atoms' distributions were affected by the investigated long-term thermal ageing. The analyses of these solute atom redistributions are presented in the following sections.

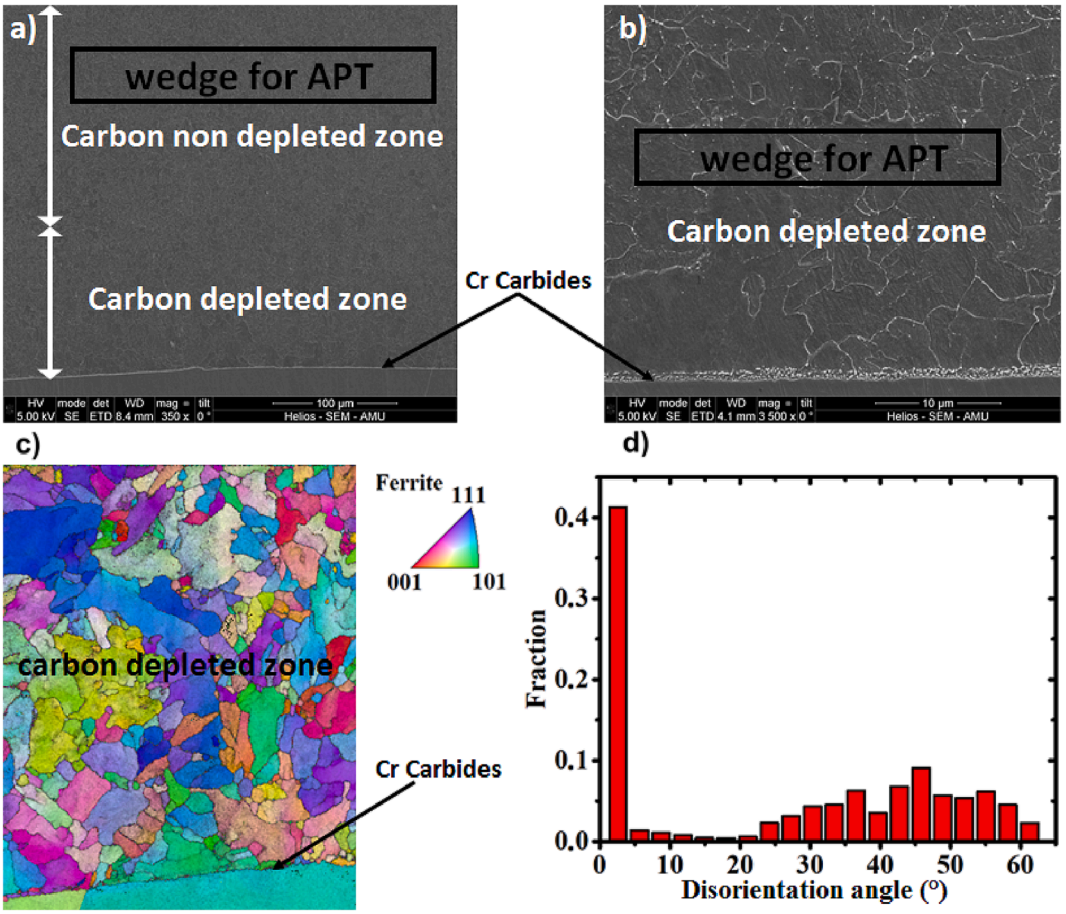

Fig. 2. A) sem image of the sample mc4–a. b) zoom on thecarbon depleted zone (CDZ) of the 18MND5 low alloy steel. c) Orientation map of grains obtained by EBSD on the same sample. d) GB disorientation angle distribution.

3.1. Investigation of the carbon-depleted zone by atom probe tomography

3.1.1. Solute atom segregation

In this part, APT results obtained on the CDZ of the five samples are presented. Bulk compositions measured by APT in the CDZ show that only a very low carbon concentration remains in solid solution (Table 3), since a significant amount of carbon atoms dissolved from carbides has diffused to the fusion line and to the nickel alloy weld metal to form chromium carbide precipitates (Fig. 3***a and 3b***).

In order to compare the long-term thermal ageing state of the different samples, a criterion considering the effect of both temperature and time must be used. Accordingly, solute atom diffusion length (L_d) is an interesting parameter [28], since segregation kinetics is diffusion dependent, and L_d takes into account both an exponential temperature effect and a root-mean-square time effect on atomic transport (***Eq. 2*** and ***3***). The average diffusion length of a given element *i*, can be calculated according to:

$$\boldsymbol{L_d^i = \sqrt{2D^i t}} \tag{2}$$

With D^i the diffusion coefficient of the considered element defined as:

$$\boldsymbol{D^i = D_0^i exp\left(-\frac{Q^i}{RT}\right)} \tag{3}$$

D_0^i and Q^i being respectively the diffusion coefficient pre-factor and the activation energy. In this work, the values of D_0^i and Q^i were extracted from the database MOBFE2 [29] included in the software DICTRA. The calculated diffusion lengths of the elements of interest are presented in Table 4. The values calculated for the sample MC4–A correspond to atomic diffusion during the SRHT. For all the other samples, the diffusion lengths correspond to the ageing times and ageing temperatures indicated in Table 2. Substitutional atom diffusion is strongly dependent on temperature in the investigated temperature and time ranges, while the effect of temperature is less discriminating for interstitial elements such as carbon. The longest C diffusion length is found in the sample MC4-C (400 °C/30 000 h).

Fig. 4 presents a reconstructed APT volume containing a GB highlighted by C, Mn, Mo, Cr, and P atomic distributions in the CDZ in the sample MC4–A (without thermal ageing). In addition to these five elements presented in this APT volume, Cu and S were also observed to have a low segregation level at the analyzed GB (Fig. 3).

Integrated profiles calculated using equation ***(1)*** are presented in Fig. 4. Eight elements (C, Mn, Ni, Mo, Cr, Cu, P and S) are found to segregate in the analyzed GB. C, Mn, and Mo are the elements exhibiting the highest segregation excess in the GB (>2 at nm^{-2}). For the other species, N_{ex} lies between 0.1 and 0.8 at nm^{-2}. The excess number values of all the segregated elements are given in Table 5**.**

At least two GBs was analyzed by APT in each aged sample. These GBs present both element segregation and phase precipitation. P segregation at GBs is shown in Fig. 5***.a b c***, the evolution of P excess segregation versus the ageing order is presented in Fig. 5.*d* using the ageing scale defined in Table 4. P segregation increases slightly according to the three ageing order with $L_d \leq 130$ nm ($N_{ex} \sim 0.7$ at.nm^{-2}). However, the P segregation level is multiplied by almost a factor 4 in the sample MC4–D ($N_{ex} \sim 2.3$ at nm^{-2}) corresponding to $L_d \sim 250$ nm. This segregation increase cannot be attributed to equilibrium segregation, as this thermal ageing treatment was performed at the highest temperature (450 °C), but is probably due to the kinetic limitation of P bulk diffusion. The two types of GBs (LAGB and HAGB) were intercepted in the sample MC4-C, corresponding to the ageing state 3. The analysis of the LAGB intercepted in this sample is presented later in Fig. 7***.c*** with C atoms represented by brown dots, highlighting the solute enrichment of the regularly spaced edge dislocations composing the LAGB [30,31]. The P segregation levels measured in the two GBs are reported in Fig. 5***d***. As expected, the P excess number is smaller in the LAGB (open circle) due to the different structure of the two GBs. Furthermore, P was shown to segregate in the core of the dislocations in LAGBs [32], which can be easily saturated, limiting P segregation.

For the other segregated solute atoms (Table 5), the behavior is not as simple to analyze, probably due to co-segregation effects. For example, C and Mn segregation increases with the ageing heat treatment order in all the specimens except in the samples MC4-2807 (order 2). This decrease could be due to co-segregation effects, but it could also suggest that the GB observed in the samples MC4-2807 is actually a LAGBs, exhibiting a total excess number of the elements about two times smaller than expected ($N_{ex} \sim 10.5$ at nm^{-2}). In general, GBs where solute segregation form a plane are considered as HAGBs. This is the case for the 2 GBs detected in the samples MC4-2807: the atomic segregation distribution in this GB forms a plane as in the case of HAGBs, and no dislocation network is observed (Fig. 7). However, one should note that for LAGBs exhibiting a disorientation angle higher than 3.5° the distance between dislocations is smaller than 4 nm, and consequently, the atomic segregation distribution also forms a plane in APT volumes. Mo atoms segregate on all the analyzed GBs. Cr and S segregate in the samples MC4–A, MC4–B and MC4–C but not in the specimens MC-2807 and MC4–D. Si atoms segregate in GBs only in the samples MC4–B, MC4–C, and MC-2807. Cu GB segregation is very different from the other solute atoms. Indeed, Cu GB segregation is only observed in the MC4–A sample (before ageing). Cu GB segregation is not observed in the other samples, however Cu-rich clusters are observed. Cu precipitation is described in the subsequent part of the paper.

Dislocation lines were also analyzed in another APT volume from the sample MC4–C. They are highlighted by Mo *iso*-concentration-surfaces in Fig. 6. The segregation of C, Mn, Si, Ni, Mo, Cr, and P is observed on these dislocation lines. These elements are the same as the elements segregating in GBs. Da Rosa *et al.* [33] proposed a method to quantify the segregation excess number on dislocation lines (N_{ex} in at nm^{-1}) from APT measurements. This method was applied in the APT volume of the sample MC4-C. The segregation excess numbers of the different elements are presented in Table 6**.** C, Mn and Mo segregation is significantly higher than the segregation of the other elements.

3.1.2. Solute atom precipitation

Cu clusters were observed in dislocation lines in all the aged samples, in addition to solute segregation *(*Fig. 6*)*. The identified clusters exhibit atomic compositions close to 45 at% of Cu, 10 at% of Mn, 1 at% of Si and 20 at% of Ni. These clusters were also observed in bulk but mainly in GBs, and are richer in Cu, Ni, Si, and Mn atoms (orange Cu *iso*-concentration in Fig. 7***.a, b***. These clusters are also present on the LAGB in the sample MC4–C as shown in Fig. 7***.c***. Finally, another class of precipitates

Table 3
Bulk compositions measured by APT (at %) in the Carbone depleted zone (CDZ).

Steels	Fe	C	Mn	Si	Ni	Mo	Cr	Cu	P	S	Al
Nominal	95.96	0.87	1.47	0.41	0.67	0.28	0.16	0.09	0.01	0.01	0.04
MC4-A	96.32	0.04	1.28	0.76	0.86	0.29	0.13	0.03	0.11	0.01	0.03
MC4-B	96.39	0.02	1.33	0.73	0.81	0.13	0.14	0.03	0.05	0.02	0.01
MC-2807	96.68	0.01	1.10	0.61	0.77	0.18	0.15	0.02	0.03	0.01	0.03
MC4-C	96.67	0.04	1.22	0.68	0.80	0.17	0.14	0.03	0.08	0.02	0.01
MC4-D	96.64	0.07	1.32	0.47	0.91	0.24	0.13	0.04	0.03	0.01	0.04

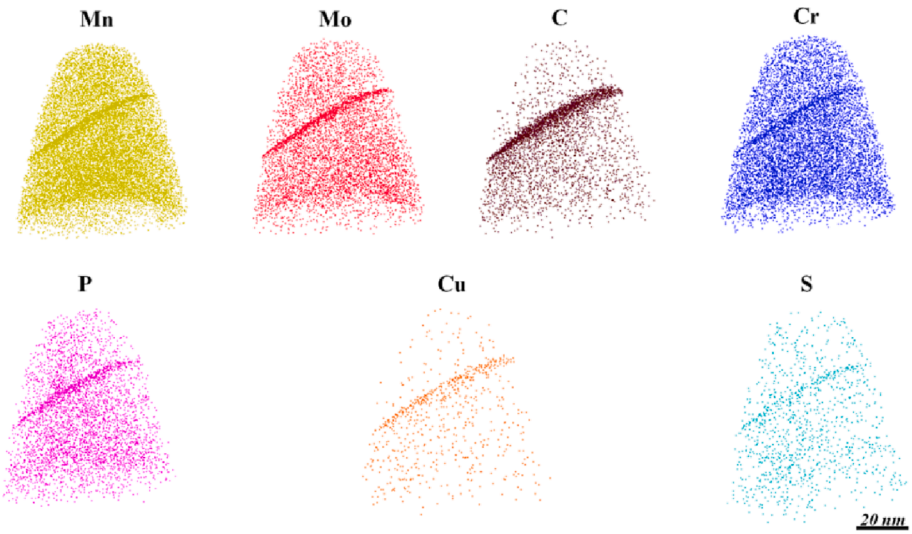

Fig. 3. Same APT volume showing Mn, Mo, C, Cr, P, Cu and S atomic distributions in the carbon depleted zone CDZ of the MC4 –A sample (without thermal ageing).

Table 4
Diffusion lengths (nm) calculated for the 5 long-term thermal ageing treatments. For the sample MC4-A, the diffusion length corresponds to the SRHT.

	Order	C	Mn	Si	Ni	Mo	Cr	Cu	P	S
MC4-A (610 °C /16 h)	0	$1.3x10^6$	259	148	146	315	103	158	623	1611
MC4-B (350 °C/50 000 h)	1	$5.8x10^6$	6.3	1.2	2.2	11.2	0.9	2.8	28.2	63
MC-2807 (400 °C/10000 h) 000 h)	2	$4.9x10^6$	19.8	5	7.8	32.1	3.6	9.6	76	176
MC4-C (400 °C/30 000 h)	3	$8.5x10^6$	34.4	8.7	13.5	55.6	6.3	16.6	132	305
MC4-D (450 °C/5 000) h)	4	$6.1x10^6$	75.5	24.2	33	112	17.3	39.1	253	604

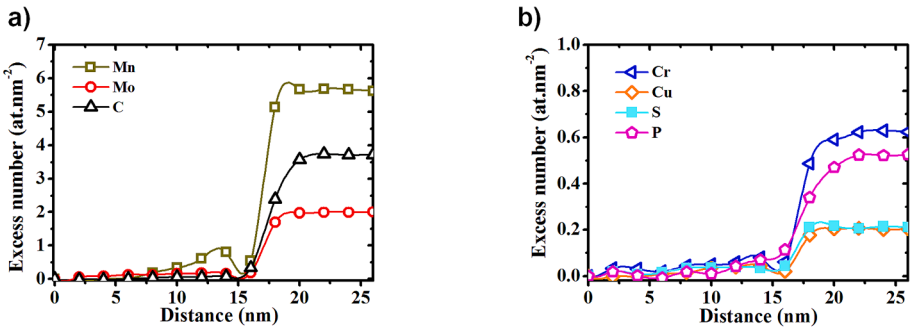

Fig. 4. Integrated profiles calculated from concentration profiles measured across a GB in the CDZ of the sample MC4-A.

Table 5
Average solute excess numbers (at.nm^{-2}) calculated from APT measurements performed on two different HAGBs for each thermal treatment. The elements are ranked from the highest to the lowest diffusion coefficient.

Steels	C	Mn	Si	Ni	Mo	Cr	Cu	P	S	Total
MC4-A	3.7 ± 1	5.6 ± 0.7	0	0	2 ± 0.1	0.6 ± 0.2	0.2 ± 0.1	0.5 ± 0.1	0.2 ± 0.1	13 ± 2.3
MC4-B	4 ± 1.2	6.2 ± 0.5	2.6 ± 0.5	1.6 ± 0.5	1.2 ± 0.1	0.67 ± 0.2	0	0.67 ± 0.01	0.25 ± 0.1	17.2 ± 2.2
MC4-2807	2.1 ± 0.4	4 ± 0.3	1.3 ± 0.5	1.2 ± 0.1	1.1 ± 0.1	0	0	0.84 ± 0.02	0	10.5 ± 1.4
MC4-C	5 ± 1	7.5 ± 0.5	1 ± 0.2	1.1 ± 0.3	5 ± 0.4	0.6 ± 0.2	0	0.88 ± 0.02	0.25 ± 0.1	20 ± 2.7
MC4-D	4.4 ± 0.4	7.8 ± 0.6	0	3.6 ± 0.2	2.6 ± 0.3	0	0	2 ± 0.3	0	21 ± 2

containing Al and N atoms was detected in HAGBs in the sample MC4–D (blue *iso*-concentration surface in Fig. 7.***d***). These precipitates contain in average 40 at% of Al, 30 at% of N, and 13 at% of Mn. It is not surprising to find AlN precipitates since Al is used to kill the steel during the steel making process.

In conclusion, the APT results show the presence of clusters in the bulk and in extended defects in the CDZ after long-term thermal ageing, while no cluster is observed in the sample MC4–A before ageing, suggesting that Cu clustering is promoted by ageing heat treatment conditions.

3.1.3. Investigations in the carbone non depleted zone

The carbon non depleted zone (CNDZ) in the sample MC4-B is investigated by APT for comparison with the results obtained in the CDZ in the same sample. The CNDZ bulk composition is compared with that of the CDZ in Table 7. The two zones have a very similar composition.

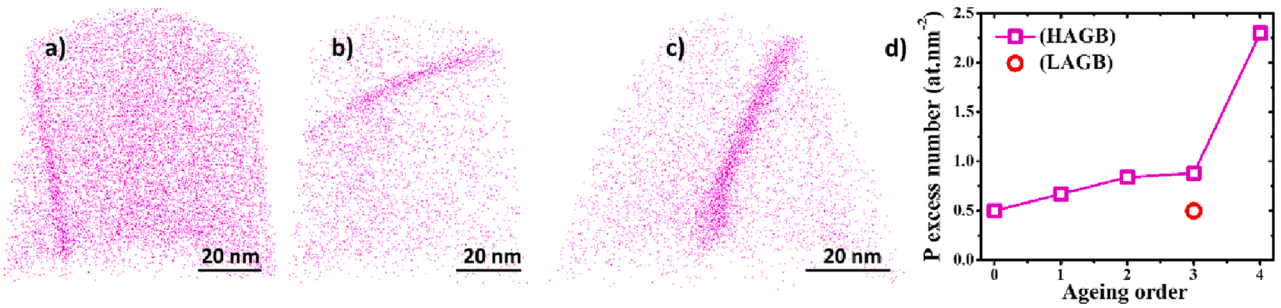

Fig. 5. APT volumes showing the P distribution in a) the sample MC4–B, b) the sample MC-2807, c) the sample MC4 –D, and d) the P segregation versus ageing using the ageing scale defined in Table 4.

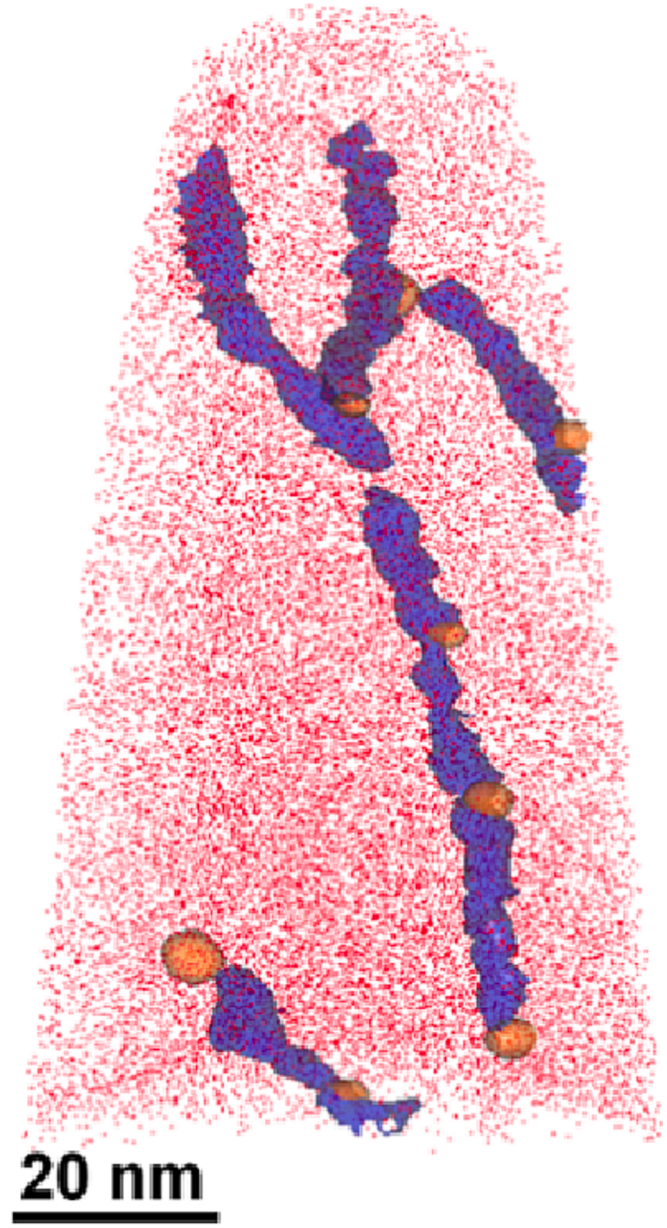

Fig. 6. APT volume measured in the sample MC4–C. Red dots correspond to Mo atoms. Mo segregation in dislocation lines is highlighted via blue *iso*-concentration surfaces, and Cu-rich precipitates are shown using orange *iso*-concentration surfaces. (For interpretation of the references to colour in this figure legend, the reader is referred to the web version of this article.)

The carbide precipitate volume density is high in the CNDZ. Thus, it is expected that the probability of intercepting a carbide precipitate during the tip preparation is high. Fig. 8.***a*** shows a GB intercepted in the CNDZ, and Fig. 8.***b*** presents the integrated profiles (***Eq. 1***) of the different segregated elements in this GB (ferrite/ferrite interface).

Six elements (C, Mn, Si, Ni, P and Mo) are found to significantly segregate in the GB, while two other elements (S and Cu) show weak segregation. The corresponding segregation excess number values are given in Table 8.

These results show that the total segregation level between the two zones (CDZ and CNDZ) is similar, as well as the P excess segregation. Nevertheless, the segregation quantities of Ni, Si, and Cr are more significant at the GBs in the CDZ compared to the CNDZ. In contrast, Mo and C GB segregation is more important in the CNDZ. These differences may be related to the different bulk composition as well as carbide distribution and density between the two zones.

The last APT volume presented in this paper shows the atomic distribution in the vicinity of an isolated dislocation in the CNDZ MC4-B, as presented in Fig. 6 in the case of the CDZ in the specimen MC4-C. Cu precipitates were also observed in dislocation lines in the CNDZ (Fig. 9). These precipitates have the following average composition: 65 at% of Cu, 6 at% of Ni, 1 at% of Si, and 7 at% of Mn. In this area, the Cu clusters are richer in Cu and less rich in Mn and Ni compared with the same type of clusters observed in the CDZ. The composition of the clusters may be affected by the different bulk composition between the two zones, but in the case of Ni, the higher Ni concentration measured in the clusters located in the CDZ is probably linked to the proximity to the Inconel weld metal acting as a Ni diffusion source.

In addition to the presence of the Cu-containing clusters, several solute elements are also segregating in the dislocation. The corresponding segregation excess numbers are gathered in Table 9. It can be noted that the elements segregating the most are again C, Mo, and Mn, as observed in isolated dislocations in the CDZ (Table 6). The total segregation excess at the dislocation lines in this zone is almost comparable to the excess measured in the dislocation lines in the CDZ (Table 9).

Several APT volumes of CNDZ bulk in the sample MC4–B were analyzed, and no Cu clusters were observed. This is a noticeable difference with the results obtained in the CDZ, where Cu-containing clusters were observed in the GBs, but mainly at dislocation lines. This result suggests that the density of the Cu-containing clusters is higher in the CDZ compared with the CNDZ due to the higher density of dislocation in the CDZ. Indeed, the cooling stage to room temperature following the welding process leads to the generation of significant stress in the region of the low-alloy steel in contact with the deposited metal. This is mainly due to the significant thermal gradients generated by the welding process as well as the difference in the coefficient of thermal expansion between the ferritic steel and the Ni-based alloy weld metal [34]. This stress promotes the formation of a high density of dislocations in the CDZ region in contact with the fusion line during cooling. The SRHT aims to release the stress and to reduce the dislocation density generated during this stage. However, the dislocation

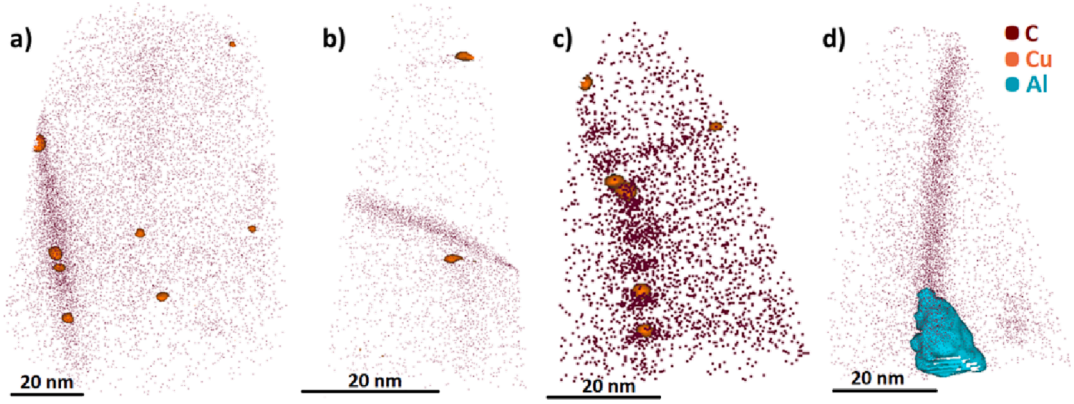

Fig. 7. APT volumes showing Cu-containing precipitates highlighted by Cu isoconcentration surfaces (1.5 at%). Brown dots show C atoms in a) the sample MC4–B, b) the sample MC-2807, c) the sample MC4–C, and d) the sample MC4–D. The blue volume in (d) corresponds to a 10% Al at isoconcentration-surface. (For interpretation of the references to colour in this figure legend, the reader is referred to the web version of this article.)

Table 6
Segregation excess number (at nm^{-1}) in the dislocation lines observed in the Sample MC4-C.

Steel	C	Mn	Si	Ni	Mo	Cr	P	Total
MC4-C	30	18	2.5	2.2	32	3	3	94

density in the CDZ remains significantly higher than in the CNDZ at the end of the SRHT.

3.2. Modelling phosphorus segregation

As recalled in the introduction of this article, P segregation to HAGBs is considered in the literature to be the main cause of long-term thermal ageing embrittlement. Our experiments show an increase of the P excess number in the CDZ when increasing the thermal ageing order (see

Table 7
ATP Bulk compositions (at%) of the carbon no depleted zone (CNDZ) and the carbon depleted zone (CDZ).

	Fe	C	Mn	Si	Ni	Mo	Cr	Cu	P	S	Al
Nominal	95.96	0.87	1.47	0.41	0.67	0.28	0.16	0.09	0.01	0.01	0.04
MC4-B CDZ	96.39	0.02	1.33	0.73	0.81	0.13	0.14	0.03	0.05	0.02	0.01
NDNDZ MC4-B CNDZ	97.14	0.02	1.13	0.45	0.85	0.15	0.13	0.04	0.03	0.01	0.01

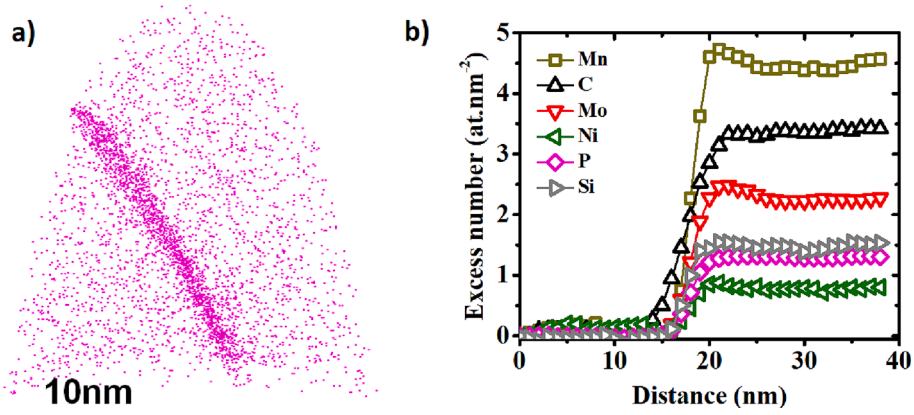

Fig. 8. APT measurements performed in the CNDZ of the sample MC4–B: a) APT volume showing the P (pink dots) atomic distribution close to a GB, and b) Integrated profiles corresponding to the different elements found to segregate in the same GB. (For interpretation of the references to colour in this figure legend, the reader is referred to the web version of this article.)

Table 8
Segregation excess numbers (at.nm^{-2}) in GBs. The species are ranked from the highest to the lowest diffusion coefficient in the two different zones (CDZ and CNDZ).

Steel	C	Mn	Si	Ni	Mo	Cr	Cu	P	S	Total
CNDZ	3.4	5	1.3	1	2.2	0	0.2	0.8	0.2	14
CDZ	4	6	1.7	1.6	1.2	0.7	0	0.7	0,2	16

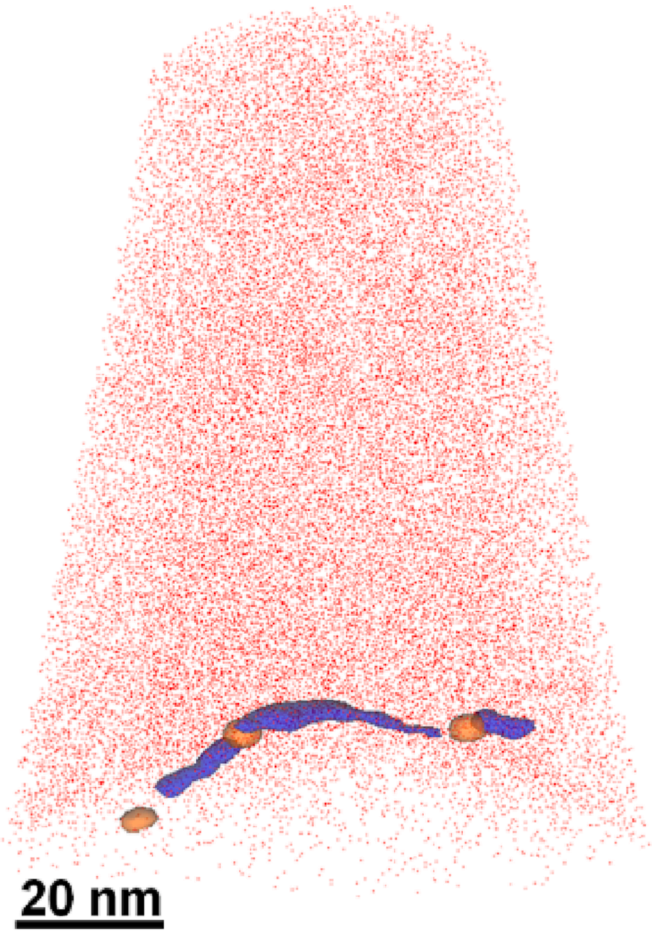

Fig. 9. APT volume from the CNDZ in the sample MC4-B (red dots correspond to Mo atoms). The blue *iso*-concentration surface shows the Mo segregation in the dislocation line, while the orange *iso*-concentration surfaces show Cu-containing precipitates on the dislocation line. (For interpretation of the references to colour in this figure legend, the reader is referred to the web version of this article.)

Table 9
Segregation excess numbers (at nm^{-1}) in the dislocation line of the specimen MC4-B intercepted in the carbon non depleted zone (CNDZ).

Steel	C	S	P	Mo	Mn	Ni	Si	Cr	Total
MC4-B	25	2	3	30	16	2	1.5	3	82.5

Table 4). However, the amounts of segregated phosphorus remain relatively low compared to other solutes (in the range of 0.5 to 2.3 at/nm^2). Furthermore, P segregation increases with temperature, which is unexpected from an equilibrium viewpoint. To check if this behavior can be understood on the basis of reasonable hypotheses, a series of calculations were performed based on mean-field modelling of the segregation kinetics.

The chosen model describes the kinetics of P atoms diffusing from the inner grain towards a planar grain boundary, during GB segregation. By computing the diffusion profiles of P as a function of time, the P flux towards the boundary is integrated, yielding the time evolution of the segregated amount. This approach presents the benefits of being possibly applied to non-isothermal heat treatments and to consider the finite size of the grains. The model is somewhat similar to that of Militzer et al. [35], although it relies on the Onsager equation of diffusion instead of Fick's law. The main features are described below. Details can be found in [36]. The P diffusion flux in the grain and in the vicinity of the boundary is written as:

$$\boldsymbol{J} = -\boldsymbol{M}\frac{\mathbf{d}\boldsymbol{\mu}}{\mathbf{d}\boldsymbol{x}} \tag{1}$$

Where M is the atom mobility, μ is the chemical potential and $\times$ is the distance to the boundary. Neglecting the P interaction with other solute atoms the alloy thermodynamics was approximated to the classical regular form:

$$\boldsymbol{\mu} = \boldsymbol{k}_{\mathrm{B}}\boldsymbol{T}\ln\frac{\boldsymbol{X}}{1-\boldsymbol{X}} + \Delta\boldsymbol{G}_{\mathrm{seg}} \tag{2}$$

Where X is the P molar fraction, k_B is the Boltzmann constant and T is the temperature. ΔG_{seg} is the Gibbs energy of segregation. It is set to zero everywhere except at the grain boundary where it is written $\Delta G_{seg} = \Delta H_{seg} - T\Delta S_{seg}$. This term builds the driving force for segregation and ensures McLean's segregation equation once local equilibrium is reached in the vicinity of the GB. The mobility M is related to the chemical diffusivity D by:

$$\boldsymbol{M} = \frac{\boldsymbol{D}}{\boldsymbol{k}_{\mathrm{B}}\boldsymbol{T}}\frac{\boldsymbol{X}(1-\boldsymbol{X})}{\boldsymbol{V}_{\mathrm{m}}} \tag{3}$$

Where V_m is the molar volume. Diffusion is thermally activated according to $D = D_0\exp(-Q/k_BT)$ with D_0 the pre-exponential term and Q the activation energy. The diffusion-segregation equations above were solved by a one-dimensional finite difference scheme, providing the diffusion profiles and the P interfacial fraction X_{seg} as function of time for a given thermal treatment. The P excess number at the GB is proportional to the interfacial fraction via the relationship $\Gamma = X_{seg}l/V_{at}$ where V_{at} is the alloy atomic volume and l is the GB thickness. The later was set to the width of two {200} planes, i.e. $L = 0.29$ nm. Accordingly, a saturated GB corresponds to an excess of 24.6 at/nm^2.

Full equilibrium between the inner grain and the GB corresponds to the case when the diffusion profile is flat across the grain (equal to X_∞) except at the boundary where it peaks to X_{seg}. The matter balance is then written $X_0 = X_\infty + V_{at}\Gamma/d$ where d is the grain size and X_0 is the P nominal molar fraction. d = 5 μm and X_0 = 130 at.ppm in the CDZ. Solving the matter balance together with McLean's equation gives the equilibrium excess number.

The diffusion profiles and P excess were computed as a function of time during the SRHT (ageing order 0) followed by the ageing treatments (orders 1, 2, 3, and 4). These treatments correspond to our experimental results on HAGBs. The P diffusion coefficient was set as the mid-value from the two independent measurements available in the literature in ferromagnetic iron [37,38], namely $D_0 = 138$ m^2/s and Q = 332 kJ/mol (Fig. 10).

A good fit to the experimental results was obtained with the

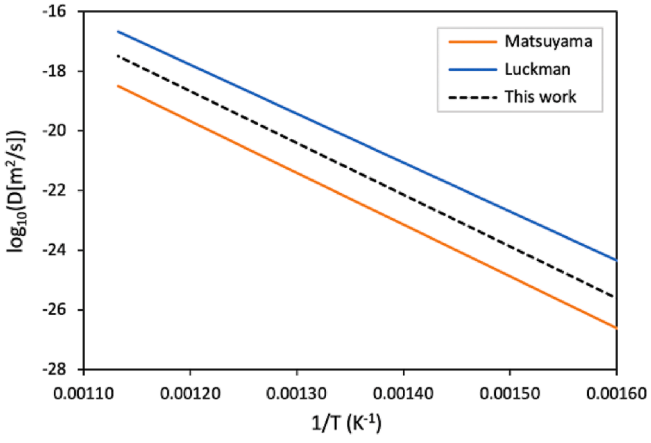

Fig. 10. P Diffusion coefficient used in the present study compared to available experimental data from Matsuyama [37] and Luckman [38].

optimized segregation parameters $E_{seg} = -0.55$ eV and $S_{seg} = -0.20$ meV K^{-1} (see Fig. 11). These values are at slight variance to the ones of Erhart et al. fitted on fully equilibrated GBs in pure Fe-P system ($E_{seg} = -0.36$ eV and $S_{seg} = 0.22$ meV K^{-1}) [39] and those fitted by Druce et al. on a quenched and tempered steel ($E_{seg} = -0.67$ eV and $S_{seg} = 0.25$ meV K^{-1}) [11], especially for the sign of the segregation entropy.

The computations confirm the low level of P segregation during ageing (Fig. 11.***a***), although the fitted segregation energy is relatively high (−0.55 eV). According to the model, the P segregation amount is far from the value attainable at full equilibrium because of the low diffusivity of P. As a consequence, P segregation exhibits a slight increase with ageing temperature, instead of the expected decrease if full equilibrium was reached after each annealing. One can also note that the segregation level (0,65 at.nm^{-2}) after the SRHT is important after both the heating and the cooling stages. The extrapolation of our calculations to the target lifetime of the EPR reactor (i.e. 60 years), considering the maximum temperature applied to the weld during service (i.e. 350 °C), leads to an excess of 0.77 at nm^{-2} Fig. 11.***b***. This value is still far from the computed equilibrium value of 5.95 at nm^{-2}. Consequently, the present simulations using parameters (D, E_{seg}, S_{seg}) extracted from experimental measurements show that P HAGB segregation is kinetically limited by P bulk diffusion during ageing and during service.

4. Discussion

As already pointed out, the microstructure obtained in the CDZ of the HAZ after the SRHT is not modified by the different long-term thermal ageing treatments. Consequently, the embrittlement reported in the work of Joly *et al* (2014) cannot be explained by the singular microstructure of the HAZ [3]. The mechanism involved with this embrittlement is thus necessarily resulting from atomic redistribution during thermal ageing, particularly in the vicinity of extended defects such as dislocations and GBs. The thermal ageing effect on the atomic distribution in the CDZ of two DMWs was then studied by APT. This zone corresponds to the zone from which tenacity toughness test curves were measured. The segregation excess numbers measured here, for different thermal ageing conditions, are to the best of the authors' knowledge, the first attempt to establish quantitative information of chemical element co-segregation at CDZ GBs that can be used in models such as the McLean model for solute element segregation. The quantitative segregation levels in GBs and dislocation lines in five samples were determined from the APT measurements. The results show that elements such as As, Sb, and Sn, which are often cited as contributors to GB embrittlement, were not detected neither in the GBs nor at the dislocations analyzed in this work. However, the precipitation of Cu-containing clusters was only observed in aged samples, mainly on structural defects. Furthermore, AlN precipitates were also observed in the most aged sample (MC4–D). However, it is not surprising to find AlN precipitates in these low alloy steels for which Al is added during steel making process to kill the steel.

The analysis of the sample MC4–A, which only experienced the SRHT, shows that GB segregation is already significant before any thermal ageing treatment (Table 5). The average diffusion length of the different elements (C, Mn, Ni, Mo, Cr, Cu, P, and S) during the SRHT (610 °C for 16 h) was calculated (Table 4) in order to better evaluate the probability of reaching the segregation equilibrium state at GBs before ageing and after ageing. The C diffusion length is large enough so that C segregation can be at equilibrium whatever the considered heat treatment. However, the diffusion coefficients of substitutional atoms are much smaller, and their diffusion lengths are shorter. Nevertheless, simple diffusion calculations show that the diffusion length of the considered substitutional elements is also sufficient to reach equilibrium segregation in each case during the SRHT. For example, a 2 nm-large depletion of Mn atoms around GBs is enough to reach the measured Mn GB excess number of 5.6 at nm^{-2}. This distance is significantly small compared with the Mn diffusion length $L_d = 259$ nm allowed during the SRHT. Knowing if the segregation has reached equilibrium in the aged sample is more complicated. It is well known that the segregation level depends on temperature. Indeed, the segregation level decreases when temperature increases [18], meaning that GB segregation in the aged samples should be higher than that in the sample MC4–A. Nevertheless, it is also well known that segregation greatly depends on the nature of the GB, and in particular on its disorientation. Considering the temperature effect, GB segregation levels are expected to be the highest at 350 °C (MC4-B sample), which is not the case in the present observations: the total segregation is more important at 450 °C (MC4-D sample) than at 350 °C (Table 5). Several hypotheses can be invoked to explain this atypical behavior. The first one is the kinetic effect: the diffusion lengths are too short to reach segregation equilibrium with the heat treatment of 50 000 h at 350 °C, for example. If we compare the diffusion lengths with the thicknesses around GBs needed to be depleted in order to reach the measured segregated values, the results are very different from one element to another. For example, the diffusion lengths are respectively 3 and 4 times larger than the needed depletion thicknesses (respectively 1.9 nm and 2.4 nm) for Mn and Mo. Segregation could have reached equilibrium for these two elements. On the contrary, for other segregated species, the diffusion lengths and the needed depletion thicknesses have really close values. Hence these species could probably not reach the GB equilibrium state at the end of the thermal treatment.

The effects of temperature and GB structure were mainly evaluated in systems for which a single element is segregating [10,40]. However, it

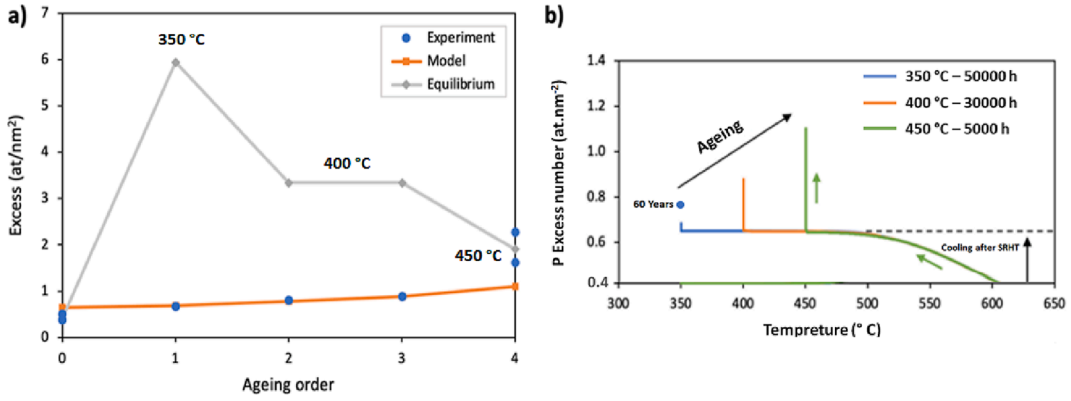

Fig. 11. P segregation kinetics in HAGBs located in the CDZ. a) Comparison between experimental and simulated excess numbers as a function of the ageing order. Two excess numbers measured by APT on two different HAGBs are given for each ageing order (blue solid circles), these data are overlapping for ageing orders 1, 2, and 3. The gray curve (solid diamonds) corresponds to equilibrium segregation. b) P excess number computed after the SRHT cooling followed by ageing at 350, 400 and 450 °C. (For interpretation of the references to colour in this figure legend, the reader is referred to the web version of this article.)

is known that interactions between segregated elements exist in complex alloys [39,41–43]. These interactions can be attractive or repulsive, and the interacting elements can have their equilibrium segregation modified. For example, our results obtained on the segregation in GBs and in dislocations show that Mn-C and Mo-C interactions are clearly attractive. This is in agreement with the tendency of Mo to form carbide precipitates or with the high solubility of Mn in cementite.

The APT results presented in this paper confirm that P does segregate in the GBs of all the analyzed samples. However, simulations using these experimental data as input parameters show that P segregation is kinetically limited by its bulk diffusion in the studied temperature range (below 450 °C). Consequently, P equilibrium GB segregation is not reached in the samples. The simulations also show that i) Heat treatments applied on the studied materials actually gives the major contribution to P GB segregation, while ii) the long-term thermal ageing treatment contribution allow a relatively small increase of the P segregation compared with the SRHT state (less than two times more at maximum at 450 °C), and iii) this contribution decreases with temperature due to the kinetic regime of segregation. However, even a small increase of P excess segregation can influence the enhancement of intergranular fracture. Furthermore, simulations of P segregation during 60 years at the maximum service temperature of 350 °C predict that P GB segregation in the CDZ heat-affected zone of the DMW should be far from equilibrium and should remain low compared with the equilibrium segregation level (0.77 at nm^{-2}, Fig. 11***)***. One can note that the P diffusion length corresponding to annealing at 350 °C for 60 years is 60 nm according to the data from DICTRA (Table 4), corresponding to a P excess of 1 $at.nm^{-2}$ on the GB if the entire amount of P located 60 nm around the GB before segregation is located on the GB after ageing, considering the P bulk concentration in our material.

A similar study was carried out on P segregation at grain boundaries in the same mock-ups but in the base metal [44]. P segregation at GBs was essentially estimated by AES. In this case, the most widely used analysis method to quantify the P segregated quantity consists in relating the phosphorus AES peak height IP120 to the iron peak height IFe703. This ratio, commonly known as the GB coverage ratio, represents the fraction of GB atomic sites occupied by P atoms. The results of Joly et al. show an increase in coverage rates as a function of temperature and ageing time [44]. Indeed, the coverage rate goes from a ratio of 0.08 for an ageing at 350 °C −50,000 h (order 1) to 0.11 for ageing at 400 °C − 30,000 h (order 3) and finally to 0.15 for ageing at 400 °C − 5000 h. These results are very interesting to compare with the results presented in the present work since the ageing conditions are the same as in our study. Although the microstructure in the CDZ of DMW differs from that of the base metal, the P segregation data measured by APT from our study can be compared with those measured by AES (Table 10), since the steel composition is similar. P excess in $at.nm^{-2}$ measured by APT can be converted into a coverage rate, similar to that obtained from AES measurements. Indeed, we can consider that the surface concentration of ferritic grains (1 0 0) N_{Fe}^{ex} is:

$$N_{Fe}^{ex} = \frac{2at}{a^2} = 24,45\ at.nm^{-2} \qquad with\ a = 0,287nm$$

With a the ferrite lattice parameter, and the number of atoms present in the plane (1 0 0) being 2 atoms per surface unit. Knowing the surface concentration of the ferritic grains (1 0 0), the coverage rate can be defined as:

$$APT\ Coverage\ ratio = N_P^{ex}/N_{Fe}^{ex}$$

With N_p^{ex} the excess measured by APT.

P/Fe ratios measured at GBs in the CDZ of DMW appear smaller than that measured by AES in the base metal. However, the trend of the P segregation according to thermal ageing order is similar for the two methods. A 3 and 2 times increase of the ratio P/Fe is respectively observed by APT and AES between the 1st and the 4th ageing orders. The intergranular fracture percentage was shown to increase with the P/Fe coverage ratio. However, a P/Fe threshold value between 0.05 and 0.1% was shown to exist below which the fracture is not intergranular [45]. This P/Fe coverage ratio limit is slightly exceeded for the ageing orders 3 and 4. However, the thermal ageing temperatures (400 and 450 °C) are well above the service temperature (320 °C) in these cases.

The P excess number (Table 5) is smaller than that of other solute elements, such as Mo, Mn, and Ni. Furthermore, element segregation excess variations compared to ageing conditions and resulting mechanical properties are not easy to understand if the analysis is only based on P segregation. For example, the two samples MC4-C and MC4-D present similar tenacity properties, though, P GB segregation is quite different in the two samples, with $N_{ex} = 0.88$ at nm^{-2} in the sample MC4-C and $N_{ex} = 2.3$ at nm^{-2} in the sample MC4-D. This is also the case for the other segregating elements, such as Mo with $N_{ex} = 5$ at nm^{-2} in the sample MC4-C and $N_{ex} = 2.6$ at nm^{-2} in the sample MC4-D, for example. Furthermore, in the not-aged sample MC4-A $N_{ex} = 0.5$ at nm^{-2} for P and $N_{ex} = 2$ at nm^{-2} for Mo. Consequently, no obvious link between GB segregation and mechanical properties can be observed.

In addition to solute segregation, clusters were also observed in the analyzed GBs in the CDZ of the MC4–B specimen. These precipitates enriched with Cu, Mn and Ni, are also observed i) in the bulk of the specimens MC4–B and MC-2807, ii) in dislocations in the CDZ of the specimen MC4–C, and in the CNDZ of the specimen MC4–B. On the contrary, these precipitates are not observed before ageing in the sample MC4–A, and after ageing in the sample MC4–D. The Cu solubility in ferrite was calculated with Thermo-Calc for $350 \leq T \leq 450$ °C. This solubility was found to be between 0.02 at% and 0.05 at%. Those values are lower than the Cu bulk nominal concentration of our material, which is 0.09 at% (Table 1). Thus, the formation of Cu clusters in the MC4 samples should indeed be expected. Small angle neutron scattering (SANS) measurements [46] already evidenced Cu precipitation at 500 °C in ferritic Fe-Cu, Fe-Cu-Mn and Fe-Cu-Ni alloys. In the two latter cases, the precipitates were also shown to contain approximately 25 at% of Mn and 25 at% of Ni, respectively. A more recent APT study [47], on a ferritic steel containing 1.82 at% of Cu, 2.67 at% of Mn, and 0.51 at% of Ni among other elements, evidenced Cu clusters containing 35–42 at% of Cu, 7–10 at% of Ni, and 1% Mn, after a heat treatment at 500 °C for 1 h. These results show that Cu clusters can form and are stable in the ferrite at least down to 500 °C. Furthermore, their absence in the sample MC4-A before ageing can be explained by thermodynamic stability. Indeed, at 610 °C, the Cu solubility is above 0.2 at% [48–50], which is higher than our sample bulk Cu composition. Long term ageing is the only difference between specimen MC4-A and the other specimens presenting Cu-rich clusters. However, before drawing any conclusion regarding the possible contribution of Cu-rich clusters in the embrittlement mechanism, more work is required since only one or two grain boundaries per specimen have been analyzed.

The last part of this discussion concerns the comparison of the decarburized and non-decarburized zones. First, the solid solution compositions of these two zones (Table 7) are nearly the same. This confirms the idea that the difference in microstructure observed between the two zones may come only from the volume fraction of carbide precipitates. In addition, the same bulk composition would mean that the level of segregation in equilibrium between GBs and grains is the same in the CDZ and the CNDZ. This hypothesis has been confirmed by comparing the level of segregation between DZ and NDZ, which shows that the

Table 10
Comparison between P/Fe coverage rates measured by two different methods (APT and AES).

Technique	Order 1	Order 3	Order 4
Coverage ratio from APT	0,03	0,04	0,1
Coverage ratio from AES [44]	0,07	0,1	0,15

same elements have segregated in GBs, almost in the same proportions, except for Mn and Cr, as these elements are also present in Fe carbides. Indeed, Mn- and Cr-rich carbide nucleation and growth on GBs lead to a decrease of Mn and Cr concentration in the GBs. In addition, the analysis of the segregation levels in dislocation lines in the CDZ of the specimen MC4–C and in the CNDZ of specimen MC4–B was also performed. The segregation excess concentrations extracted from these two samples are gathered in Table 6 and Table 9, respectively. The same chemical elements segregate equally in both samples at dislocations as well as in GB: C, Mn, Si, Ni, Mo, Cr, Cu, P and S. However, a quantitative analysis reveals that the elements segregating the most in dislocations and GBs are C, Mo, Mn and Ni. Again, GB segregation being roughly the same in both the CDZ and the CNDZ, its correlation with the preferential fracture in the CDZ highlighted by the analysis of the fractured surfaces is not obvious. Other factors, such as grain size [51,52] (bigger size in the CDZ) or the proximity with the fusion line (transition zone with different mechanical properties), may also play a role in locating the crack propagation of tenacity toughness specimens in the CDZ. One can note that the density of Cu clusters is significantly higher in the CDZ than in the CNDZ. Indeed, our results show that Cu precipitation occurs mainly on dislocations and the dislocation density is higher in the CDZ. However, as already mentioned, more work is needed in order to establish the influence of Cu-rich clusters on long-term thermal ageing embrittlement, since only few studies were yet performed on the presence of theses precipitates after long-term ageing heat treatment [52–55].

5. Conclusion

APT was used to study GB segregation in the heat affected zone of dissimilar metal welds, in order to explain the preferential fracture propagation in the CDZ often observed. As expected, Charpy impact tests confirm that thermal ageing leads to an embrittlement of the DWM. This APT study, focused on GBs segregation in the CDZ of DMW specimens before and after thermal ageing, shows that in addition to P, other elements such as C, S, Mn, Si, Ni, Mo, Cr, and Cu also segregate to GBs, as well as to other extended defects such as dislocations.

The APT results show that the total excess segregation at the GBs increases after long-term thermal ageing treatment. In the case of P that is considered as the main cause of the HAZ embrittlement under thermal ageing, the amount segregated increases with ageing. However, the increase of Mn and Ni segregation that is also known for lowering GB cohesion may also play a role on intergranular embrittlement. Furthermore, the segregation of other elements, such as Mo and C, which can improve GB cohesion is also observed. The contribution of GB segregation on mechanical property variations observed before and after thermal ageing is not obvious due to the combination of interactions and effects of the different solutes. The APT experimental data were used to model and simulate P segregation in HAGBs. The simulations not only show that P segregation is kinetically limited by bulk diffusion, but also that P segregation increases with temperature. The ageing heat treatments allow an increase of P segregation compared with the post heat treatment in this kinetic regime of segregation. Furthermore, the simulations predict that P GB segregation in the carbon-depleted heat-affected zone of the DMW should remain low compared with the equilibrium segregation level during the entire EPR^{TM} reactor service. This work is a first attempt to quantitatively characterize GB segregation of multiple elements. A meaningful and quantitative value such as the excess concentration for each segregating element can be used to study GB co-segregation. However, more APT work is needed to obtain more representative excess concentration values, since only two grain boundaries were analyzed in each specimen. In addition to these findings, the APT measurements highlighted the presence of Cu-containing clusters in GBs, dislocations, and bulk, only in specimens submitted to thermal ageing. These clusters are quite small, with a size between 2 and 5 nm. Their composition varies between the CDZ and the CNDZ, with a Cu composition of 45–70 at%, a Ni composition of 6–20 at%, and a Mn composition of 7–10 at%. The presence of these clusters seems to be more significant in the CDZ than in the CNDZ. However, the effect of these clusters on the material mechanical properties in not clear yet.

CRediT authorship contribution statement

I. Medouni: Investigation, Visualization, Writing – review & editing. **A. Portavoce:** Conceptualization, Visualization, Supervision, Validation, Writing – review & editing, Project administration. **P. Maugis:** Conceptualization, Investigation, Methodology, Software, Validation, Writing – review & editing. **M. Descoins:** Investigation. **M. Yescas:** Funding acquisition, Resources, Supervision, Writing – review & editing. **F. Roch:** Funding acquisition, Resources. **P. Joly:** Funding acquisition, Resources, Writing – review & editing. **K. Hoummada:** Conceptualization, Visualization, Supervision, Validation, Writing – review & editing, Project administration, Funding acquisition.

Declaration of Competing Interest

The authors declare that they have no known competing financial interests or personal relationships that could have appeared to influence the work reported in this paper.

Data availability

All the necessary data is available in the main text. Any other relevant data are also available upon request, except the full original POS files obtained from APT measurements, since these set of data contain additional information unrelated to the subject of this study, which are the property of FRAMATOME.

Acknowledgments

This project was supported by the National Association of Research and Technology (ANRT – Project n°2018/1472).

References

[1] M. Guttmann, The link between equilibrium segregation and precipitation in ternary solutions exhibiting temper embrittlement, Metal Science 10 (1976) 337–341, https://doi.org/10.1179/030634576790431390.
[2] P. Lejček, M. Šob, V. Paidar, Interfacial segregation and grain boundary embrittlement: an overview and critical assessment of experimental data and calculated results, Prog. Mater Sci. 87 (2017) 83–139, https://doi.org/10.1016/j.pmatsci.2016.11.001.
[3] P. Joly, M. Yescas, E. Keim, Fracture toughness in the ductile-brittle transition and thermal ageing behavior of decarburized heat affected zone of alloy 52 dissimilar metal welds of nuclear components, in: American Society of Mechanical Engineers, Pressure Vessels and Piping Division (Publication) PVP, American Society of Mechanical Engineers (ASME), 2014, https://doi.org/10.1115/PVP2014-29044.
[4] M. Yescas, P. Joly, F. Roch, Thermal aging assessment and microstructural investigations of alloy 52 dissimilar metal welds for nuclear components, American Society of Mechanical Engineers, Pressure Vessels and Piping Division (Publication), PVP. (6B–2019 (2019)) 1–9, https://doi.org/10.1115/PVP2019-93120.
[5] Z. Zhai, Y. Miyahara, H. Abe, Y. Watanabe, Segregation behavior of phosphorus in the heat-affected zone of an A533B/A182 dissimilar weld joint before and after simulated thermal aging, J. Nucl. Mater. 452 (2014) 133–140, https://doi.org/10.1016/j.jnucmat.2014.05.005.
[6] A.M. Remmal, V. Paraskevaidis, S. Marie, A. Blouin, S. Chapuliot, Prediction of ductile crack growth in a narrow gap Inconel dissimilar weld, Int. J. Press. Vessel. Pip. 173 (2019) 94–100, https://doi.org/10.1016/j.ijpvp.2019.05.002.
[7] D. Darmawan, Welding and Fabrication Technology for new Power Plant, in: J Chem Inf Model, Welding and Fabrication Technology for new Power Plants, 2019: pp. 1689–1699. doi: 10.1017/CBO9781107415324.004.
[8] M. Yamaguchi, Y. Nishiyama, H. Kaburaki, Decohesion of iron grain boundaries by sulfur or phosphorous segregation: First-principles calculations, Phys. Rev. B: Condens. Matter Mater. Phys. 76 (2007), https://doi.org/10.1103/PhysRevB.76.035418.
[9] S. Hong, S.Y. Shin, J. Lee, C.H. Lee, S. Lee, Effect of phosphorous and boron addition on microstructural evolution and Charpy impact properties of high-phosphorous-containing plain carbon steels, Mater. Sci. Eng. A 564 (2013) 461–472, https://doi.org/10.1016/j.msea.2012.11.102.

[10] H. Nakata, K. Fujii, K. Fukuya, R. Kasada, A. Kimura, Grain boundary phosphorus segregation in thermally aged low alloy steels, J. Nucl. Sci. Technol. 43 (2006) 785–793, https://doi.org/10.1080/18811248.2006.9711160.
[11] S.G. Druce, G. Gage, G. Jordan, Effect of ageing on properties of pressure vessel steels, Acta Metall. 34 (1986) 641–652, https://doi.org/10.1016/0001-6160(86)90179-3.
[12] M.A. Islam, M. Novovic, P. Bowen, J.F. Knott, Effect of phosphorus segregation on fracture properties of 2.25Cr-1Mo pressure vessel steel, J. Mater. Eng. Perform. 12 (2003) 244–248, https://doi.org/10.1361/105994903770343079.
[13] I. Medouni, A. Portavoce, P. Maugis, M. Yescas, F. Roch, P. Joly, A. Compos, C. Dominici, K. Hoummada, Effect of thermal ageing on atomic redistribution at the ferrite/ferrite and ferrite/cementite interfaces, J. Mater. Sci. 55 (25) (2020) 11561–11571.
[14] G.F. Vander Voort, Properties and Selection: Irons, Steels, and High-Performance Alloys, ASM, in: Properties and Selection: Irons, Steels, and High-Performance Alloys, ASM International, 1990, pp. 689–736.
[15] J.P. Bailon, F. Weinberg, Segregation at melted grain boundaries in steel, Can. Metall. Q. 19 (1980) 251–257, https://doi.org/10.1179/cmq.1980.19.2.251.
[16] S.H. Song, Y. Zhao, Y. Cui, J. Sun, H. Si, J.Q. Li, Effect of grain boundary character distribution and grain boundary phosphorus segregation on the brittleness of an interstitial-free steel, Mater. Lett. 182 (2016) 328–331, https://doi.org/10.1016/j.matlet.2016.07.023.
[17] J.E. Castle, Practical surface analysis by Auger and X-ray photoelectron spectroscopy. D. Briggs and M. P. Seah (Editors). John Wiley and Sons Ltd, Chichester, 1983, 533 pp., £44.50, Surface and Interface Analysis. 6 (1984) 302–302. doi: 10.1002/sia.740060611.
[18] P. Lejcek, Grain Boundary Segregation in Metals 136 (2010), https://doi.org/10.1007/978-3-642-12505-8.
[19] K. Seto, D.J. Larson, P.J. Warren, G.D.W. Smith, Grain boundary segregation in boron added interstitial free steels studied by 3-dimensional atom probe, Scr. Mater. 40 (1999) 1029–1034, https://doi.org/10.1016/S1359-6462(98)00485-0.
[20] D. Raabe, M. Herbig, S. Sandlöbes, Y. Li, D. Tytko, M. Kuzmina, D. Ponge, P. P. Choi, Grain boundary segregation engineering in metallic alloys: A pathway to the design of interfaces, Curr. Opin. Solid State Mater. Sci. 18 (2014) 253–261, https://doi.org/10.1016/j.cossms.2014.06.002.
[21] A.J. Wilkinson, T. ben Britton, Strains, planes, and EBSD in materials science, Materials Today. 15 (2012) 366–376. doi: 10.1016/S1369-7021(12)70163-3.
[22] S.I. Wright, M.M. Nowell, S.P. Lindeman, P.P. Camus, M. de Graef, M.A. Jackson, Introduction and comparison of new EBSD post-processing methodologies, Ultramicroscopy 159 (2015) 81–94, https://doi.org/10.1016/j.ultramic.2015.08.001.
[23] Standard FIB lift-out sample preparation procedure for APT, (2015). www.cameca.com (accessed March 31, 2022).
[24] P. Maugis, K. Hoummada, A methodology for the measurement of the interfacial excess of solute at a grain boundary, Scr. Mater. 120 (2016) 90–93, https://doi.org/10.1016/j.scriptamat.2016.04.005.
[25] W.T. Read, W. Shockley, Dislocation models of crystal grain boundaries, Physical, Review 78 (1950) 275–289, https://doi.org/10.1103/PhysRev.78.275.
[26] J.P. Hirth, Jens. Lothe, Theory of dislocations, 2nd ed., Wiley, New York, 1982.
[27] B. Eghbali, EBSD study on the formation of fine ferrite grains in plain carbon steel during warm deformation, Mater. Lett. 61 (2007) 4006–4010, https://doi.org/10.1016/j.matlet.2007.01.019.
[28] P. Paufler, Landolt-Börnstein, Zeitschrift Fur Kristallographie - New Crystal Structures. (1993), https://doi.org/10.1524/zkri.1993.204.Part-1.159.
[29] MOBFE2 Mobility Database & Thermo-Calc AB. MOBFE2., (1999).
[30] L. Zhang, B. Radiguet, P. Todeschini, C. Domain, Y. Shen, P. Pareige, Investigation of solute segregation behavior using a correlative EBSD/TKD/APT methodology in a 16MND5 weld, J. Nucl. Mater. 523 (2019) 434–443, https://doi.org/10.1016/j.jnucmat.2019.06.002.
[31] J.C.M. Li, Some elastic properties of an edge dislocation wall, Acta Metall. 8 (1960) 563–574, https://doi.org/10.1016/0001-6160(60)90111-5.
[32] I. Medouni, A. Portavoce, P. Maugis, P. Eyméoud, M. Yescas, K. Hoummada, Role of dislocation elastic field on impurity segregation in Fe-based alloys, Sci. Rep. 11 (2021), https://doi.org/10.1038/s41598-020-80140-4.
[33] G. da Rosa, P. Maugis, J. Drillet, V. Hebert, K. Hoummada, Co-segregation of boron and carbon atoms at dislocations in steel, J. Alloy. Compd. 724 (2017) 1143–1148, https://doi.org/10.1016/j.jallcom.2017.07.096.
[34] L. Halbauer, A. Buchwalder, R. Zenker, H. Biermann, The influence of dilution on dissimilar weld joints with high-alloy TRIP/TWIP steels, Welding in the World. 60 (2016) 645–652, https://doi.org/10.1007/S40194-016-0324-X.
[35] M. Militzer, J. Wieting, Theory of segregation kinetics in ternary systems, Acta Metall. 34 (1986) 1229–1236, https://doi.org/10.1016/0001-6160(86)90009-X.
[36] G. da Rosa, P. Maugis, A. Portavoce, J. Drillet, N. Valle, E. Lentzen, K. Hoummada, Grain-boundary segregation of boron in high-strength steel studied by nano-SIMS and atom probe tomography, Acta Mater. 182 (2020) 226–234, https://doi.org/10.1016/j.actamat.2019.10.029.
[37] T. Matsuyama, H. Hosokawa, H. Suto, Tracer Diffusion of P in iron and iron alloys, Trans. Jpn. Inst. Metals 24 (1983) 589–594, https://doi.org/10.2320/matertrans1960.24.589.
[38] G. Luckman, R.A. Didio, W.R. Graham, Phosphorus interdiffusivity in α-Fe binary and alloy systems, Metall. Trans. A 12 (1981) 253–259, https://doi.org/10.1007/BF02655198.
[39] H. Erhart, H.J. Grabke, Equilibrium segregation of phosphorus at grain boundaries of Fe–P, Fe–C–P, Fe–Cr–P, and Fe–Cr–C–P alloys, Metal Science 15 (9) (1981) 401–408.
[40] M. Paju, H. Viefhaus, H.J. Grabke, Phosphorus segregation in austenite in Fe-P-C, Fe-P-B and Fe-P-C-B alloys, Steel Research. 59 (1988) 336–343, https://doi.org/10.1002/srin.198801524.
[41] M. Guttmann, Interfacial Segregation in Multicomponent Systems, NATO Conference Series, (Series) 6, Mater. Sci. 5 (1983) 465–494, https://doi.org/10.1007/978-1-4613-3500-9_17.
[42] M. Guttmann, Equilibrium segregation in a ternary solution: A model for temper embrittlement, Surf. Sci. 53 (1975) 213–227, https://doi.org/10.1016/0039-6028(75)90125-9.
[43] M. Guttmann, P. Dumoulin, M. Wayman, The thermodynamics of interactive co-segregation of phosphorus and alloying elements in iron and temper-brittle steels, Metall. Trans. A 13 (1982) 1693–1711, https://doi.org/10.1007/BF02647825.
[44] P. Joly, F. Roch, L. Sun, Investigation of Thermal Aging of RPV Steel (type RCC-M 16-18MND5 base metals and welds), aged in laboratory furnace be-tween 350°C and 450°C, n.d. Framatome intern report.
[45] C. Naudin, J.M. Frund, A. Pineau, Intergranular fracture stress and phosphorus grain boundary segregation of a Mn-Ni-Mo steel, Scr. Mater. 40 (9) (1999) 1013–1019.
[46] F. Maury, N. Lorenzelli, C.H. de Novion, Influence of Mn and Ni on Cu precipitation in dilute iron alloys during electron irradiation: A small-angle neutron scattering study, J. Nucl. Mater. 183 (1991) 217–220, https://doi.org/10.1016/0022-3115(91)90491-O.
[47] H.H. Wang, Z. Tong, T.P. Hou, K.M. Wu, T. Mehmood, Effects of evolution of nanoscale copper precipitation and copper content on mechanical properties of high-strength steel weld metal, Sci. Technol. Weld. Join. 22 (2017) 191–197, https://doi.org/10.1080/13621718.2016.1213583.
[48] D.A. Curry, Grain-size dependence of cleavage fracture toughness in mild steel [5], Nature 276 (1978) 50–51, https://doi.org/10.1038/276050a0.
[49] S.A. Khan, M.A. Islam, Influence of prior austenite grain size on the degree of temper embrittlement in Cr-Mo steel, J. Mater. Eng. Perform. 16 (2007) 80–85, https://doi.org/10.1007/s11665-006-9012-0.
[50] J.A.G.& R.M.F. G.R. Speich, Diffusivity and Solubility Limit of Copper in Alpha and Gamma Iron, The Electron Microprobe, John Wiley and Sons Inc. (1966) 525–542.
[51] M. Perez, F. Perrard, V. Massardier-Jourdan, X. Kleber, V. Schmitt, A. Deschamps, Low Temperature Solubility Limit of Copper in Iron, Mater. Sci. Forum 500–501 (2005) 631–638, https://doi.org/10.4028/www.scientific.net/msf.500-501.631.
[52] J.E. Zelenty, Understanding thermally induced embrittlement in low copper RPV steels utilising atom probe tomography, Mater. Sci.and Technology (United Kingdom). 31 (2015) 981–988, https://doi.org/10.1179/1743284714Y.0000000718.
[53] P.D. Styman, J.M. Hyde, A. Morley, K. Wilford, N. Riddle, G.D.W. Smith, The effect of Ni on the microstructural evolution of high Cu reactor pressure vessel steel welds after thermal ageing for up to 100,000 h, Mater. Sci. Eng. A 736 (2018) 111–119, https://doi.org/10.1016/j.msea.2018.08.063.
[54] K. Lindgren, M. Boåsen, K. Stiller, P. Efsing, M. Thuvander, Cluster formation in in-service thermally aged pressurizer welds, J. Nucl. Mater. 504 (2018) 23–28, https://doi.org/10.1016/j.jnucmat.2018.03.017.
[55] Q. Liu, J. Gu, Hierarchical Cu precipitation in lamellated steel after multistage heat treatment, Phil. Mag. 97 (2017) 2361–2374, https://doi.org/10.1080/14786435.2017.1341649.